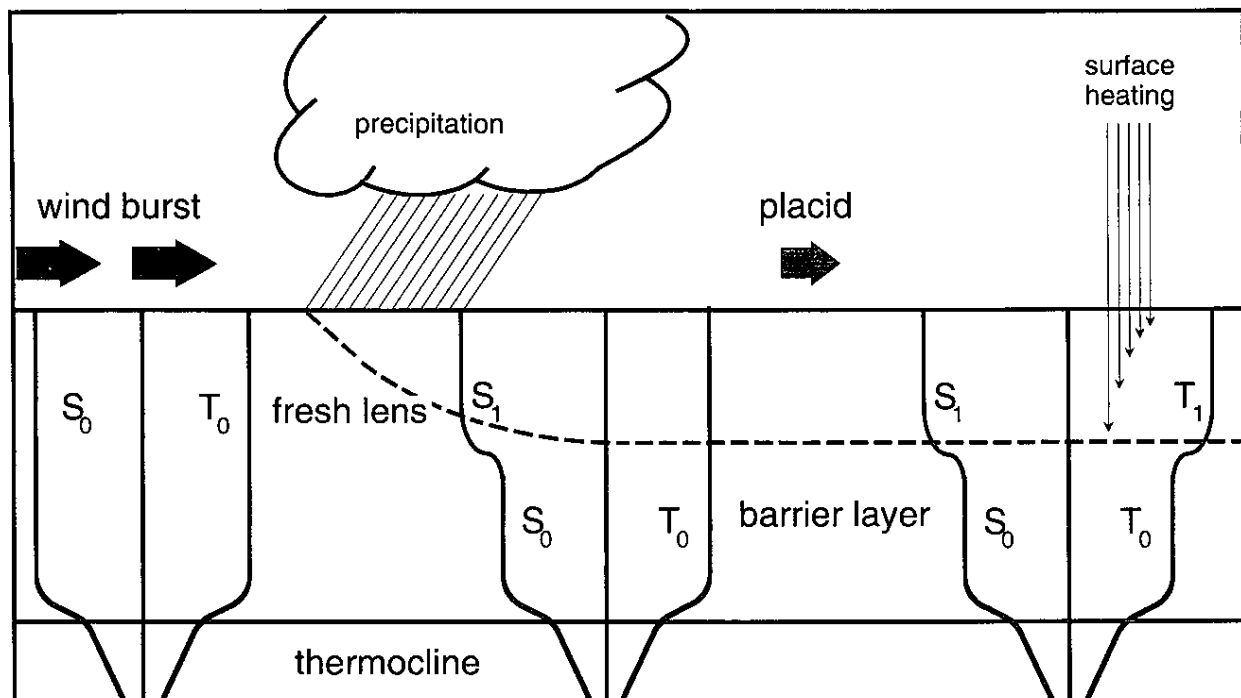
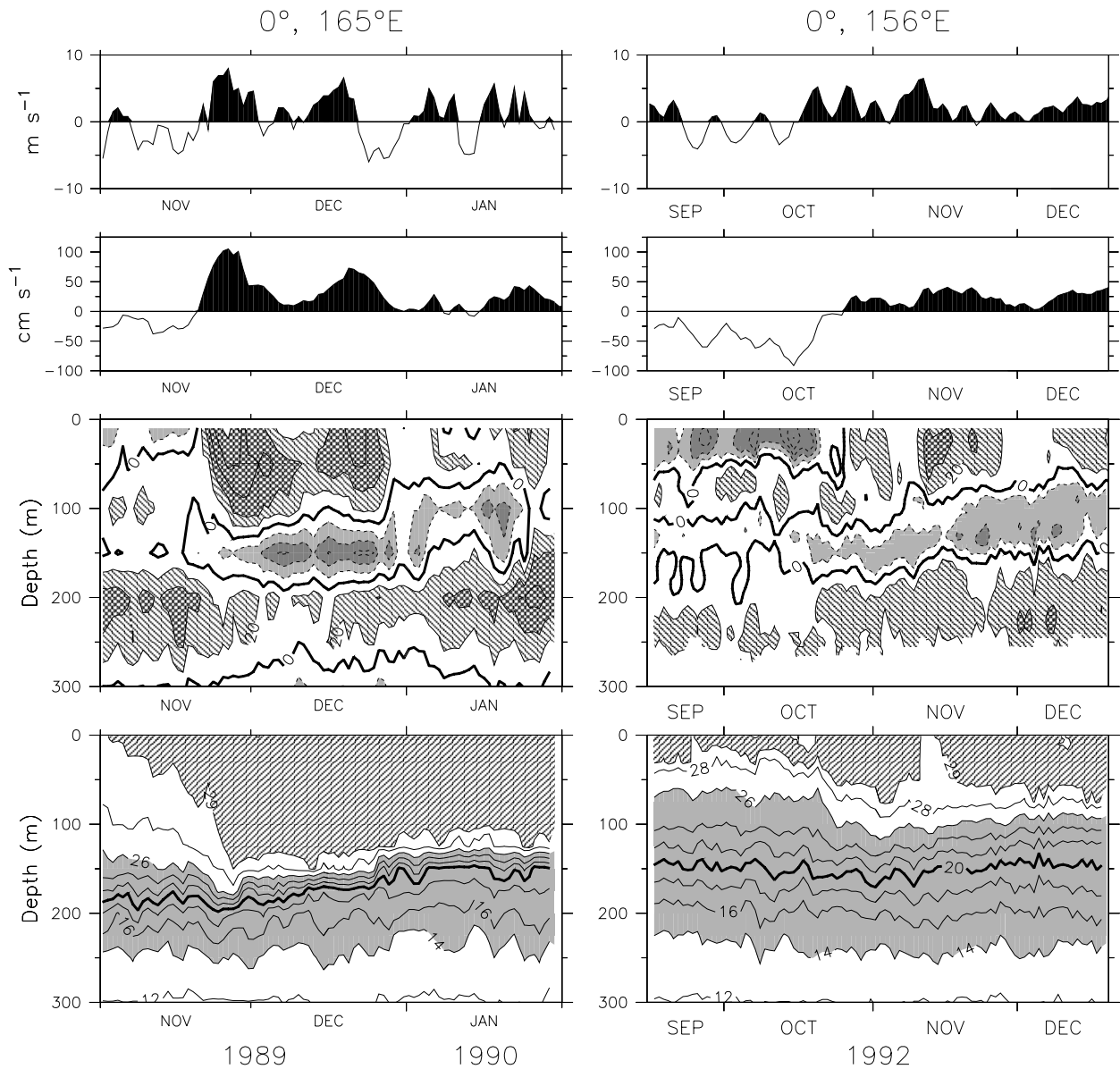


**Figure 6.1**



**Figure 6.1.** Schematic diagram showing the Lukas-Lindstrom “barrier layer” theory. During a strong wind burst, the surface mixed layer extends down to the top of the thermocline. Following the wind burst, the additional buoyancy from precipitation and strong surface heating acts to form a relatively warm and fresh thin surface layer. Below this thin layer is a strong halocline, which effectively decouples the surface forcing from the deeper waters. Further heating is trapped to vertical mixing above the barrier formed by the halocline. (After Anderson *et al.*, 1996).

**Figure 6.2**



**Figure 6.2.** Zonal wind (top), 10m zonal current (upper middle), zonal current (lower middle) and temperature (bottom) at  $0^{\circ}$ ,  $165^{\circ}\text{E}$  during 1989-1990 (left panels) and at  $0^{\circ}$ ,  $156^{\circ}\text{E}$  during 1992 (right panels). In the upper panels westerly winds and eastward currents are shaded. In the lower middle panels hatching indicates eastward currents, gray-shading westward currents, with a contour interval of  $20 \text{ cm s}^{-1}$ . In the bottom panels, hatching indicates temperatures greater than  $29^{\circ}\text{C}$ , and gray-shading indicates the thermocline with temperatures between  $14^{\circ}\text{C}$  and  $26^{\circ}\text{C}$ .

**Figure 6.3**

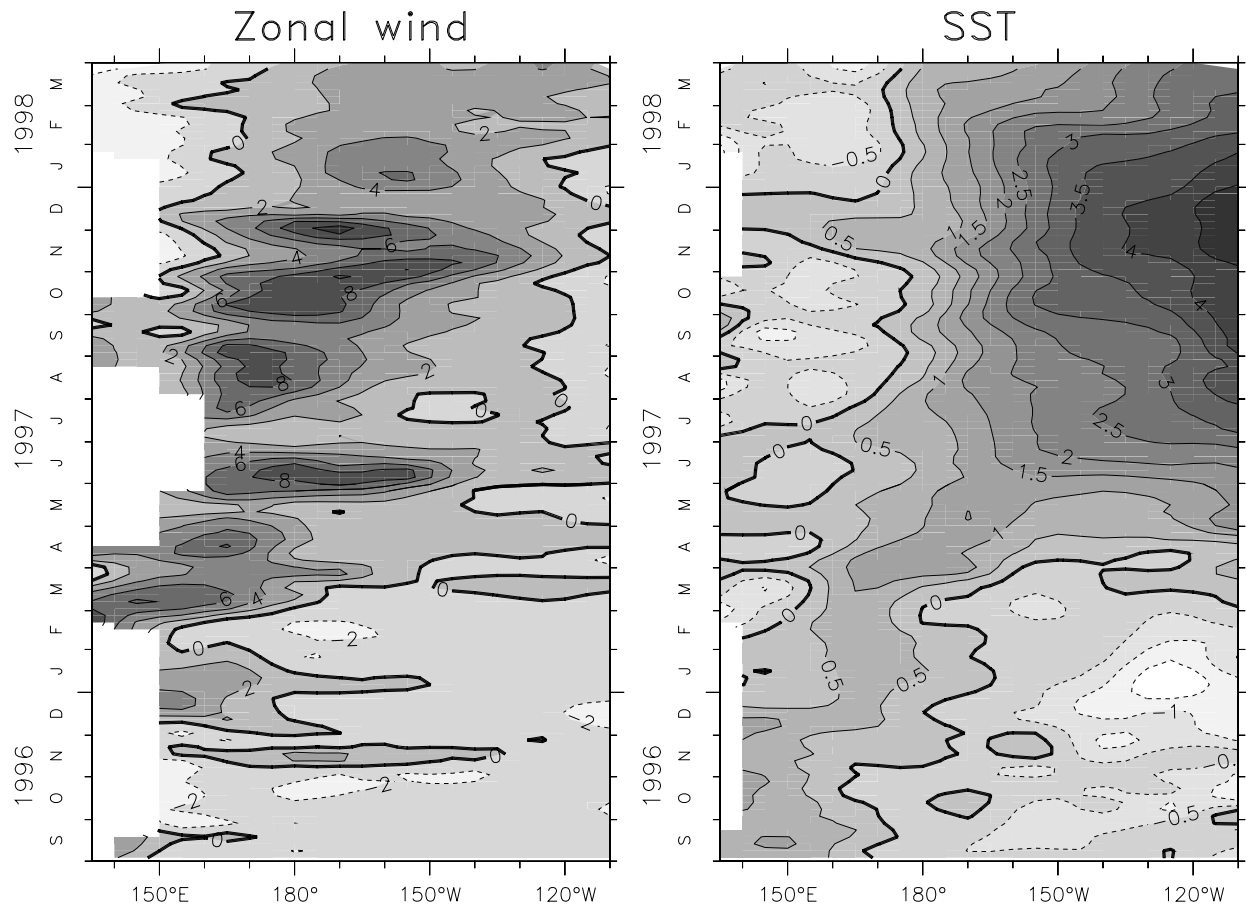


**Figure 6.3.** Zonal wind (left) and SST (right) anomalies along the equator, based on data from TAO moorings. Dark shading and solid contours indicate westerly wind and high SST anomalies. Contour intervals are  $2 \text{ m s}^{-1}$  and  $0.5^\circ\text{C}$ .

**Figure 6.4**

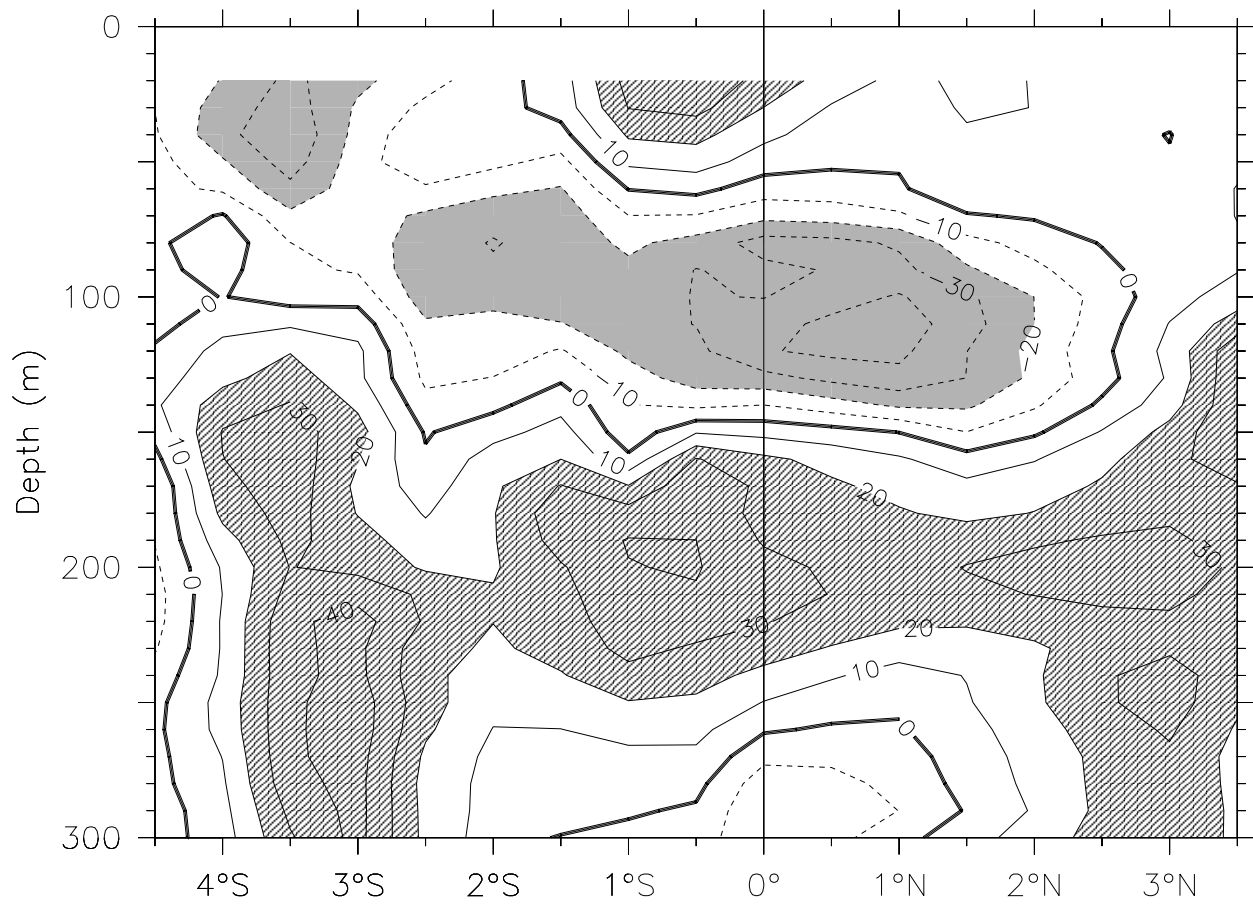


**Figure 6.4.** Zonal current example illustrating the subsurface westward jet (SSWJ) sandwiched between a frictional surface eastward current and the eastward Equatorial Undercurrent at 200 m. Hatching and solid contours indicate eastward current, gray-shading and dashed contours indicate westward current. The contour interval is  $10 \text{ cm s}^{-1}$ . The measurements were made by shipboard ADCP along  $156^\circ\text{E}$  during 8-11 December 1992, from the R/V Le Noroit. Only data while the ship was on-station was used to construct the section.

**Figure 6.5**

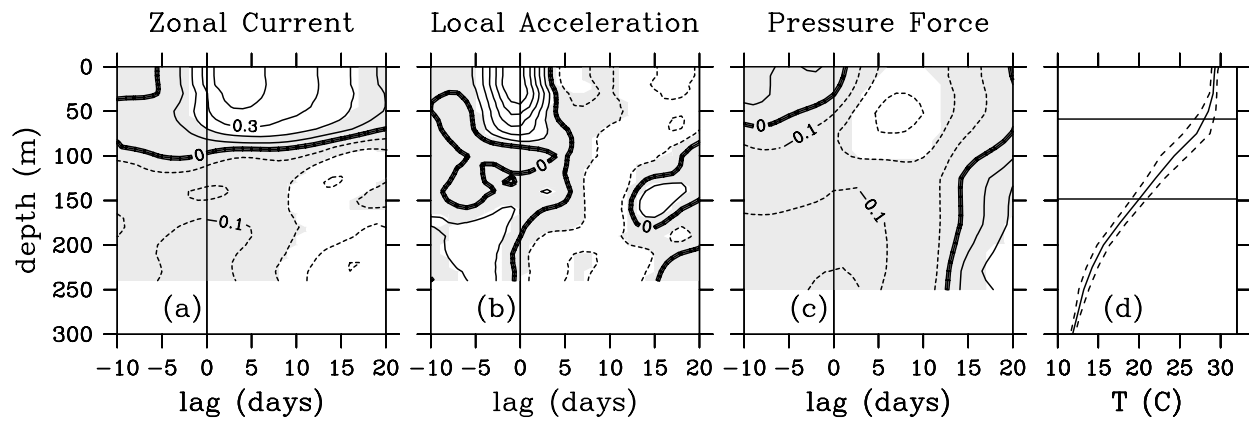


**Figure 6.5.** Lagged correlation between local zonal wind stress and (a) zonal current, (b) local zonal current acceleration, and (c) zonal pressure gradient force as a function of depth at 0°, 156°E. A positive lag implies that wind stress variability occurs prior to the respective variable anomaly. (d) Mean temperature and its standard deviation envelope at 0°, 156°E. The two horizontal lines show the mean depths of the 28°C and 20°C isotherms, which define the surface, intermediate and Equatorial Undercurrent layers. Correlations that are not significant at the 90% confidence level are shaded. The contour interval is 0.1. (After Cronin *et al.*, 2000).

**Figure 6.6**

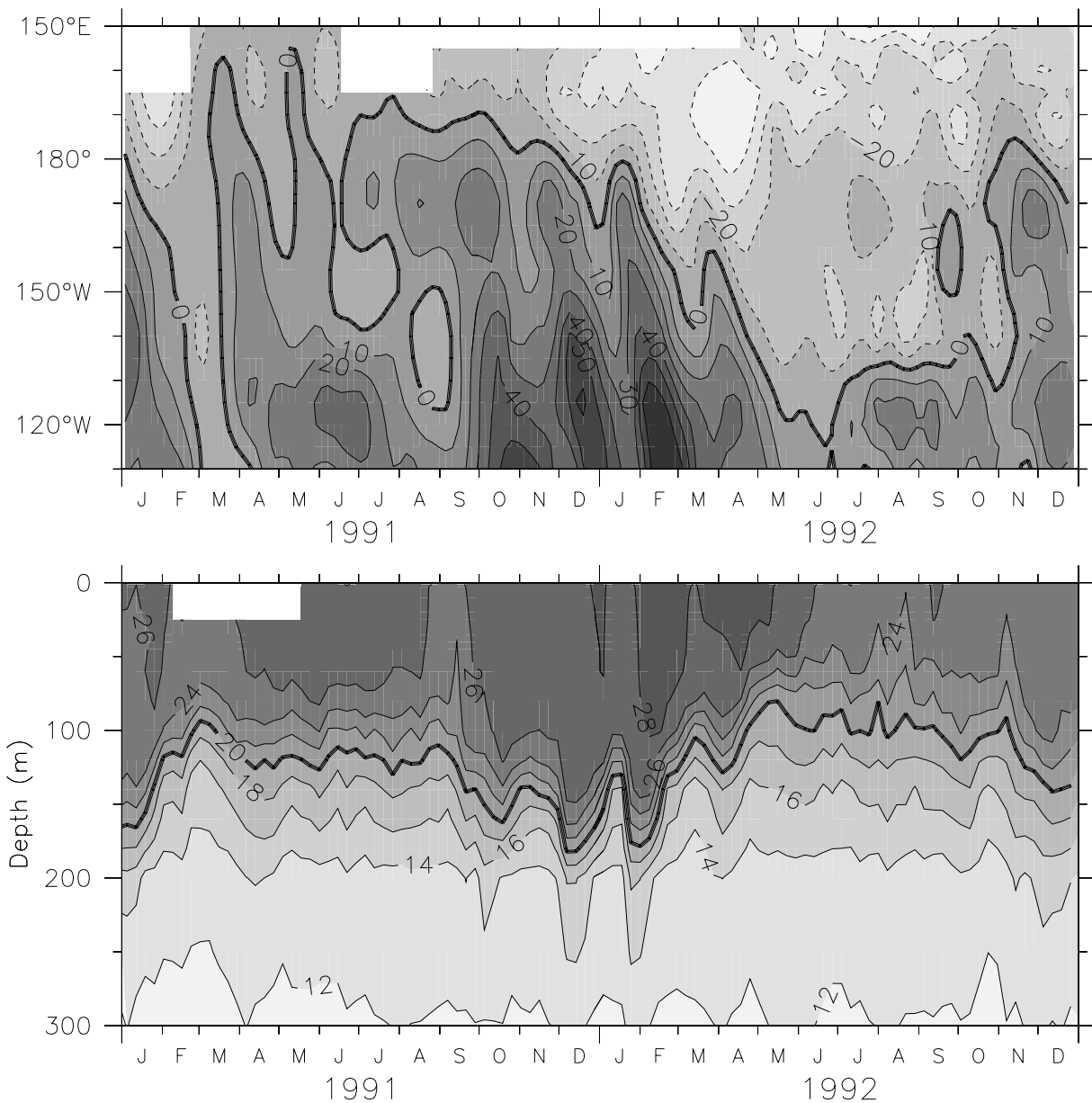


**Figure 6.6.** Top: Anomalous depth of the 20°C isotherm along the equator. Dark shading indicates deep anomalies, with a contour interval of 10m. The intraseasonal Kelvin waves are evident as tilted bands, especially during Sep. 1991 through Feb. 1992. Bottom: Temperature at 0°, 140°W. Dark shading indicates higher temperature, with a contour interval of 2°C. The 20°C isotherm is shown as the thick line. Kelvin waves arriving from the western Pacific produce the sharp downwelling events. For both panels, data comes from TAO moorings.

**Figure 6.7**

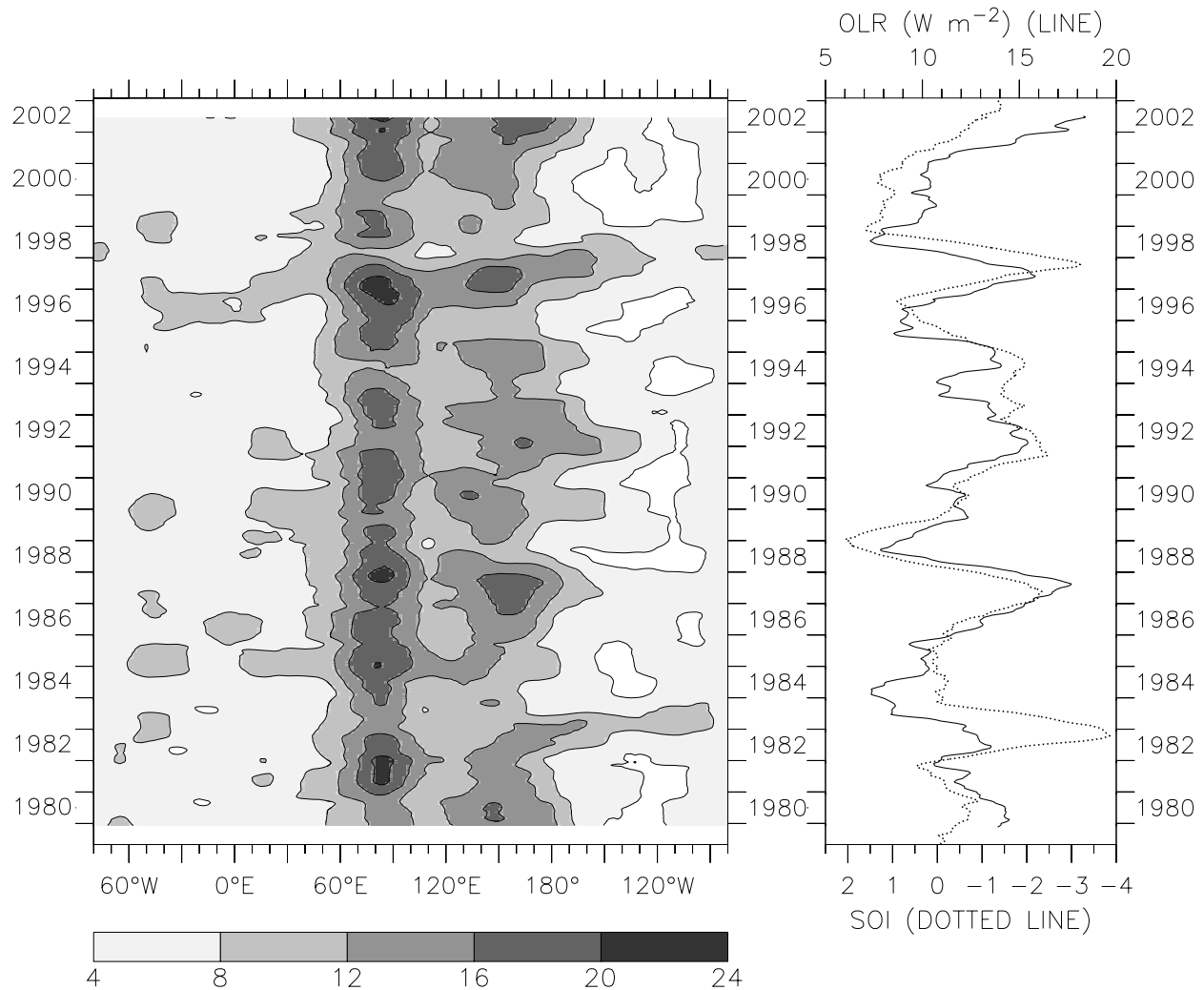


**Figure 6.7.** Interannual amplitude of intraseasonal OLR ( $5^{\circ}\text{S}$ - $5^{\circ}\text{N}$ ) ( $\text{W m}^{-2}$ ), defined as the one-year running standard deviation of intraseasonally-bandpassed OLR. (Left) Amplitude in the global tropical strip, centered on the major region of variance at  $100^{\circ}\text{E}$  (the abscissa extends around the world, broken at the South American coast at  $80^{\circ}\text{W}$ ). (Right) Time series of OLR amplitude averaged over the western Pacific ( $150^{\circ}\text{E}$ - $180^{\circ}$ ) (solid line, scale at top) in comparison with the SOI (dotted line, scale at bottom). Year ticks on each panel are at 1 January of each year, with year labels centered at mid-year. (After Kessler, 2001).

**Figure 6.8**

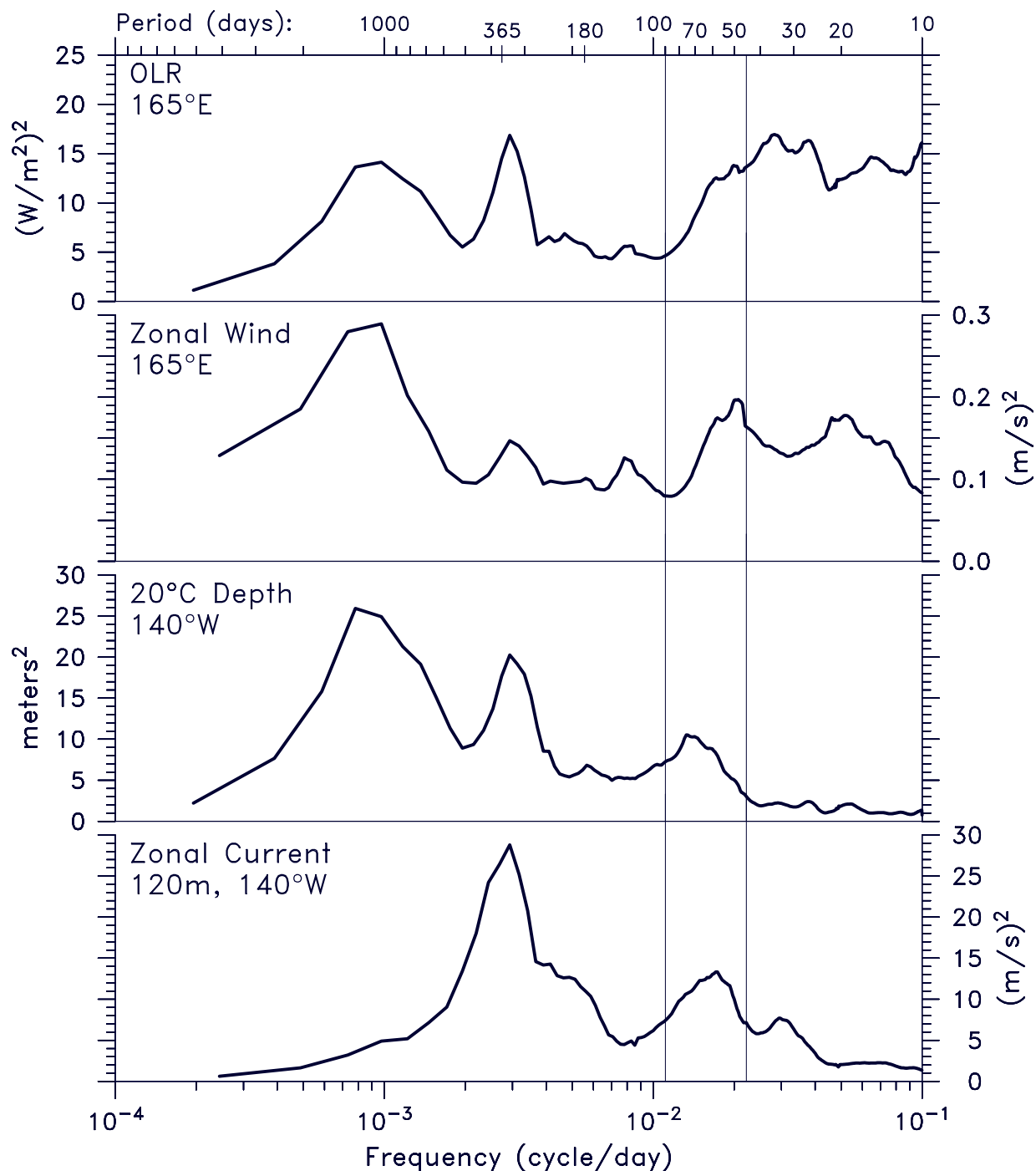


**Figure 6.8.** Variance-preserving spectra of OLR at 165°E, zonal wind at 165°E, 20°C depth at 140°W, and Equatorial Undercurrent speed at 140°W, 120 m depth, all at the equator. Each variable has a separate scale as indicated. The spectra are calculated for the 10-year period April 1983-April 1993 for all quantities except zonal wind, for which only the 7 years July 1986 - July 1993 were available. (After Kessler *et al.*, 1995).



**Figure 6.9**

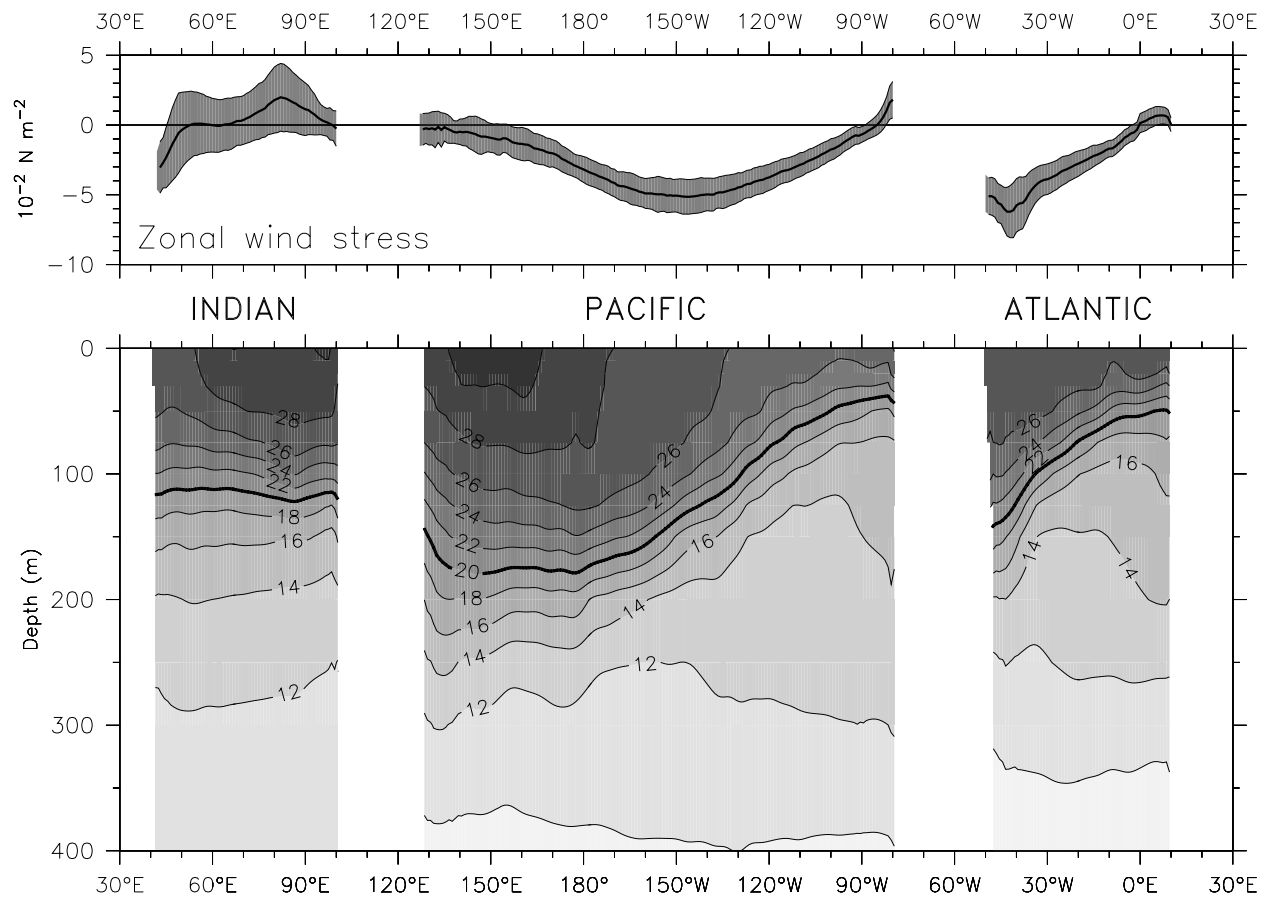


**Figure 6.9.** Mean zonal wind stress (top) and upper ocean temperature (bottom) along the equator. The winds are from the ERS scatterometer during 1992 through 2000, averaged over 5°S-5°N. The heavy line shows the mean, and the gray shading around it shows the standard deviation of the annual cycle. The ocean temperatures are from the Levitus (1994) World Ocean Atlas, with a contour interval of 2°C, and a supplemental contour at 29°C

**Figure 6.10**

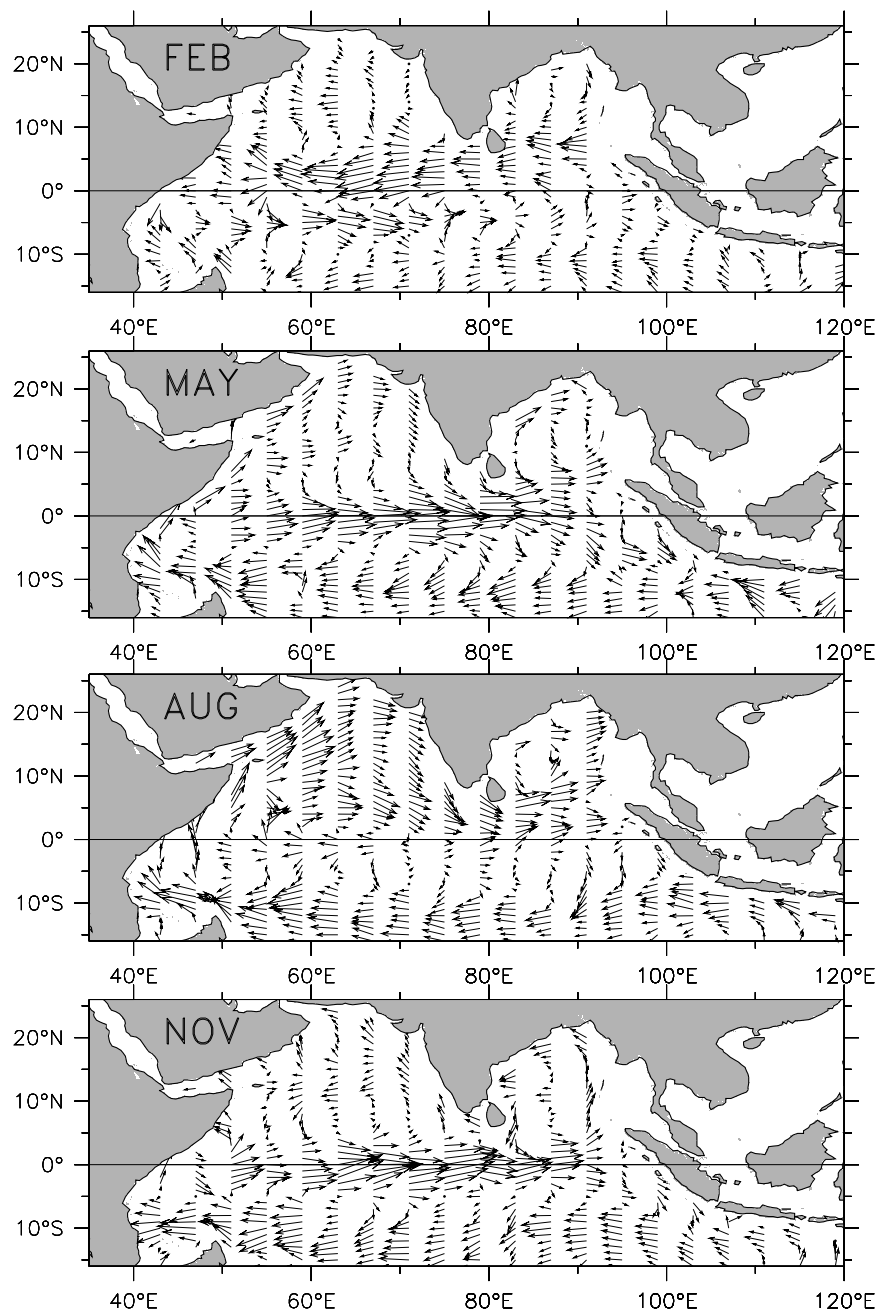


**Figure 6.10.** Seasonal cycle of Indian Ocean surface currents from historical ship-drift data (Mariano *et al.*, 1995). North of about 8°S the annual and semi-annual variation of most currents is much larger than the mean. The Wyrki Jets are the equatorially-trapped eastward currents during May and November. The dramatic seasonal reversals of circulation in the Arabian Sea, the Bay of Bengal, and along the African Coast (Somali Current) are also evident.

**Figure 6.11**

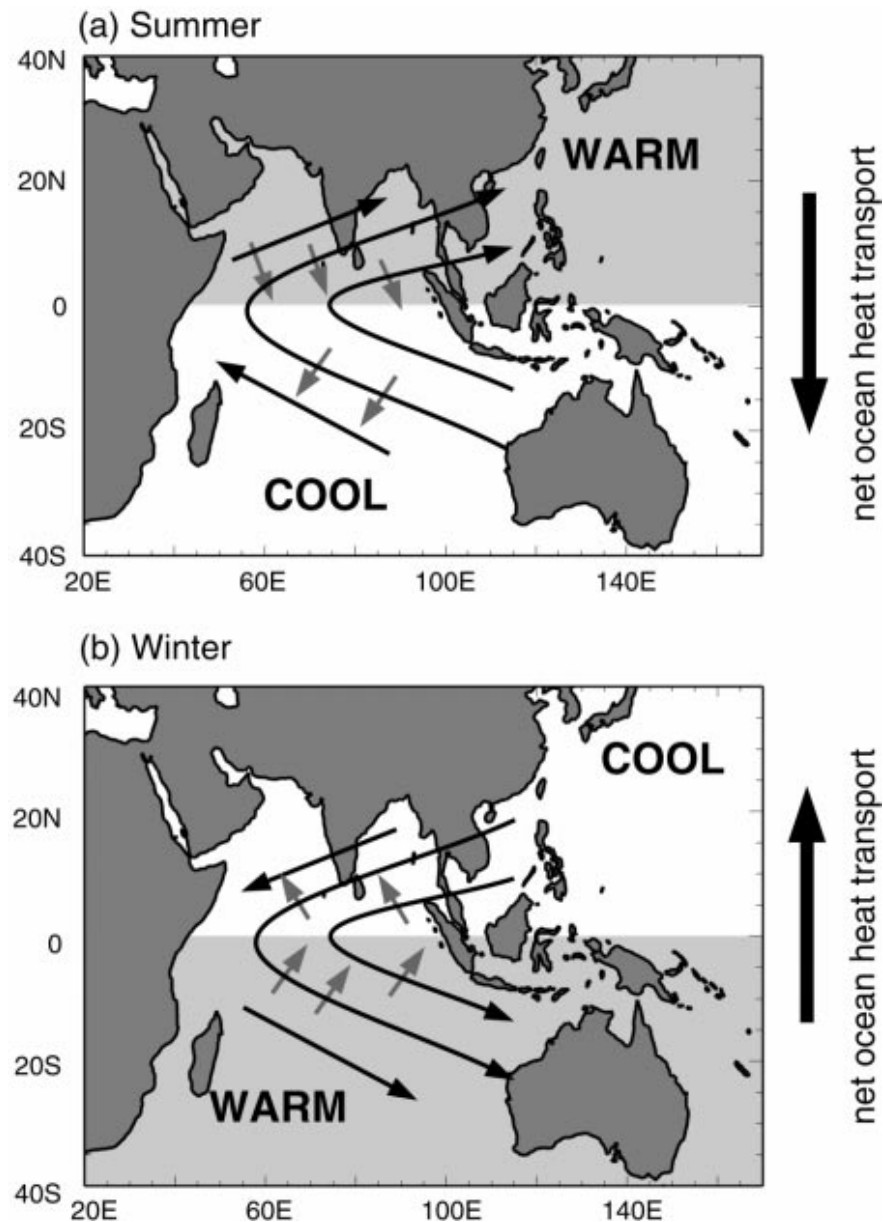


**Figure 6.11.** A regulatory model of the annual cycle of the Indian Ocean monsoon system depicted for (a) summer (Jun-Sep) and (b) winter (Dec-Feb). Curved black arrows denote the wind forced by the large-scale differential heating denoted by “warm” and “cool”. The small gray arrows are the Ekman transport forced by the winds. The large vertical black arrows to the right show the net ocean heat transport that reverses between summer and winter. The net effect of the combined wind-forced ocean circulation is to transport heat to the winter hemisphere, thus modulating the SST differences between the hemispheres. (After Loschnigg and Webster, 2000).

**Figure 6.12**

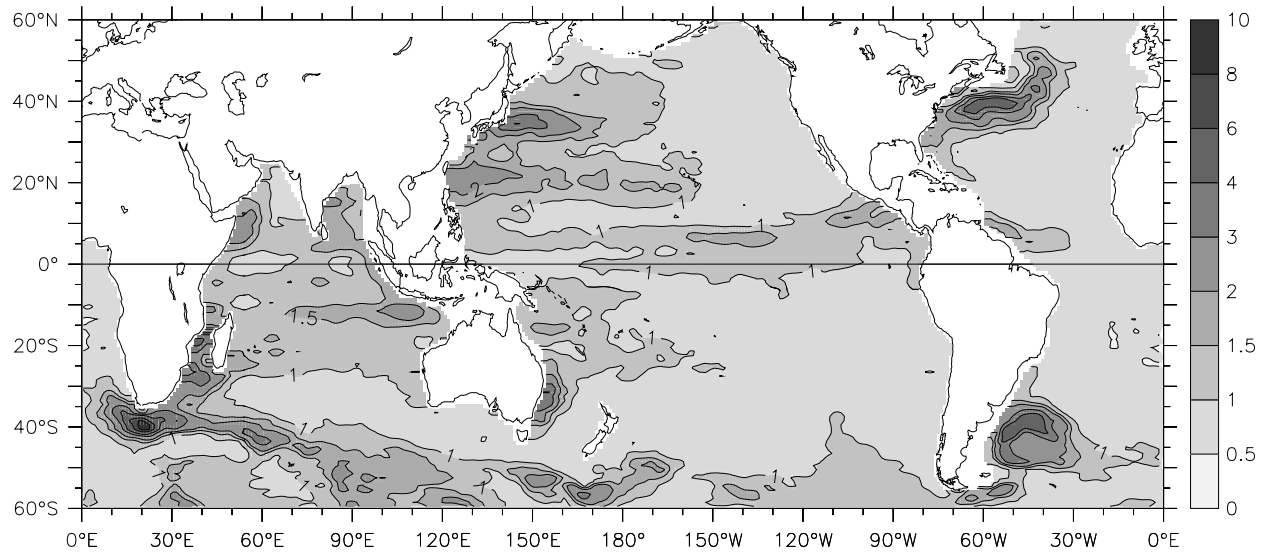


**Figure 6.12.** RMS of band-passed (35 to 85-day half power) sea level from the TOPEX/Poseidon satellite altimeter, for data during January 1992 through July 2003. Dark shading indicates high sea level RMS, with a stretched contour interval (values indicated in the scale at right).

**Figure 6.13**

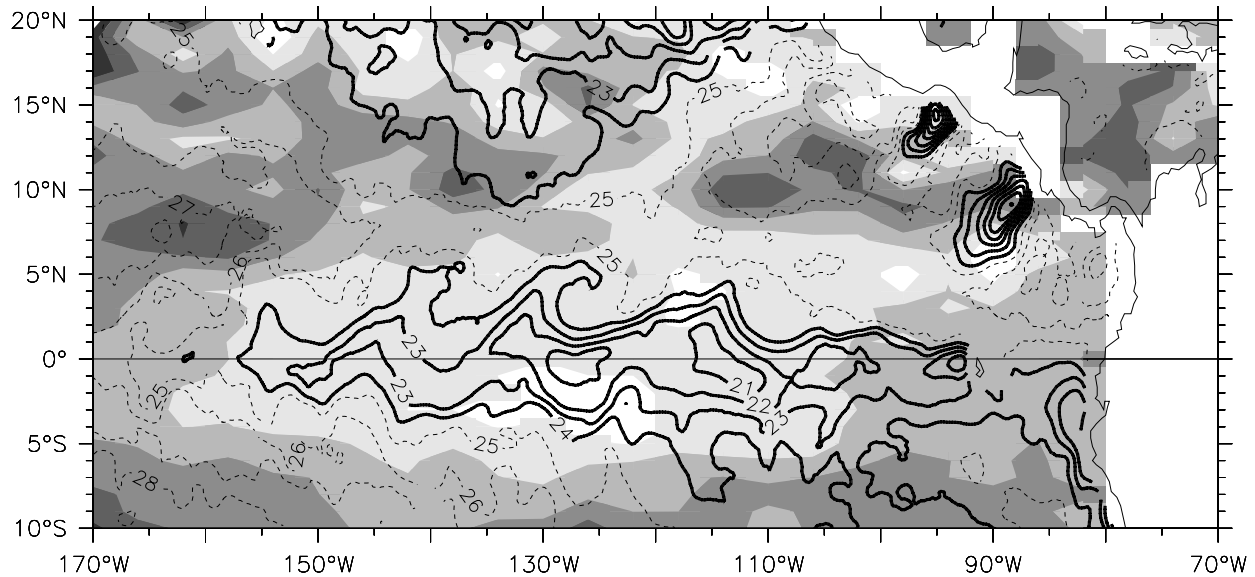


**Figure 6.13.** Example of the sea surface topography (shading) and temperature (contours) observed by satellite during January 2000, illustrating the signatures of the Central American eddies and of the tropical instability waves (section 6.7.2). The eddies are visible as the four dark patches lined up along 8°N-12°N; these are warm-core (anticyclonic) vortices produced by episodic mountain-gap winds through the Central American Cordillera. They propagate west with a speed of about  $15 \text{ cm s}^{-1}$  ( $400 \text{ km month}^{-1}$ ). The direct SST effects of the winds are seen as the packed dark (cool) contours that indicate the location of the strongest winds at Tehuantepec and Papagayo. The dark SST contours along the equator show the cold tongue (SST greater than  $25^\circ\text{C}$  is indicated by dashed contours). The cusps along the tight SST gradient on the north side of the tongue are the signature of tropical instability waves. These waves propagate west with a speed of about  $50 \text{ cm s}^{-1}$  ( $1000 \text{ km month}^{-1}$ ).